Inorganic Chemistry
Article

Inorg. Chem. **2009**, *48*, 10553–10559 **10553**
DOI: 10.1021/ic900927j

In Situ Powder X-ray Diffraction, Synthesis, and Magnetic Properties of the Defect Zircon Structure $ScVO_{4-x}$

Shahid P. Shafi,[†] Matthew W. Kotyk,[†] Lachlan M. D. Cranswick,[‡] Vladimir K. Michaelis,[†] Scott Kroeker,[†] and Mario Bieringer*[,†]

[†]*Department of Chemistry, University of Manitoba, Winnipeg, Manitoba, Canada R3T 2N2, and* [‡]*Canadian Neutron Beam Centre, National Research Council Canada, Chalk River Laboratories, Chalk River, Ontario, Canada K0J 1J0*

Received May 12, 2009

We report the formation pathway of $ScVO_4$ zircon from $ScVO_3$ bixbyite with emphasis on the synthesis and stability of the novel intermediate defect zircon phase $ScVO_{4-x}$ ($0.0 < x \leq 0.1$). The formation pathway has been investigated by means of thermogravimetric/differential thermal analysis and in situ powder X-ray diffraction. The oxidation of $ScVO_3$ to $ScVO_4$ involves two intermediates of composition $ScVO_{3.5+y}$ ($0.00 \leq y \leq 0.22$) and the novel phase $ScVO_{4-x}$. $ScVO_{4-x}$ crystallizes in the defect zircon structure in space group $I4_1/amd$ (141) with a = 6.77761(5) Å and c = 6.14045(8) Å. Oxygen defect concentrations in bulk $ScVO_{4-x}$ samples range from $0.0 < x \leq 0.1$. $ScVO_{4-x}$ is compared with the fully oxidized zircon structure $ScVO_4$ using powder X-ray diffraction, neutron diffraction, and bulk magnetic susceptibility data as well as ^{45}Sc and ^{51}V solid state NMR spectroscopy. $ScVO_{4-x}$ can only be obtained by oxidation of $ScVO_3$ or $ScVO_{3.5+y}$ while the reduction of $ScVO_4$ does not yield the novel defect structure. Mechanistic insights into the oxidative formation of $ScVO_4$ via the defect structure are presented.

1. Introduction

Rare earth orthovanadates of compositions AVO_4 with pentavalent vanadium and AVO_3 with trivalent vanadium have been extensively studied due to their interesting magnetic, optical, and electronic properties[1−6] along with potential applications in secondary lithium ion batteries[7] and photocatalysis.[8] We are primarily interested in vanadate redox chemistry with compounds of composition AVO_x where vanadium is the only paramagnetic cation in oxidation states V^{3+} (d^2 ions → $S = 1$) and V^{4+} (d^1 ions → $S = 1/2$) in the presence of a trivalent diamagnetic A-cation. The solid state oxidation pathway of AVO_3 (A = rare-earth or rare-earth like) bixbyite to AVO_4 zircon is of particular interest because of the structural relations between oxidation intermediates and the parent AVO_3 and AVO_4 phases. The AVO_3 structure types are primarily determined by the A^{3+} cation sizes. Lu^{3+} is the smallest known A^{3+} cation capable of forming a stable AVO_3 perovskite structure whereas smaller A^{3+} cations such as Sc^{3+} and In^{3+} form bixbyite phases[9−11] with A^{3+}/V^{3+} disorder on the two available octahedral cation sites. AVO_4 (where A = La−Lu, Sc, Y) compounds are isostructural with the tetragonal zircon phase, $ZrSiO_4$ (space group $I4_1/amd$). In zircon type $ScVO_4$, each Sc ion is coordinated to eight oxygen atoms in a dodecahedral fashion, and the vanadium ion is coordinated to four oxide ions forming VO_4 tetrahedra. The AVO_4 series has been investigated especially for their magnetic,[12] luminescent,[13] and photocatalytic[8] properties. The unit cell volumes of the AVO_4 phases scale with the A^{3+} cation sizes. Furthermore, a systematic decrease of the V−O

*To whom correspondence should be addressed. E-mail: mario_bieringer@umanitoba.ca. Phone: (204) 474-6258. Fax: (204) 474-7608.

(1) Dorogova, M.; Navrotsky, A.; Boatner, L. A. *J. Solid State Chem.* **2007**, *180*, 847.
(2) Nguyn, H. C.; Goodenough, J. B. *Phys. Rev. B* **1995**, *52*, 324–334.
(3) Mizokawa, T.; Khomskii, D. I.; Sawatzky, G. A. *Phys. Rev. B* **1999**, *60*, 7309.
(4) Ren, Y.; Palstra, T. T. M.; Khomskii, D. I.; Pellegrin, E.; Nugroho, A. A.; Menovsky, A. A.; Sawatzky, G. A. *Nature* **1998**, *396*, 441.
(5) Miyasaka, S.; Okimoto, Y.; Iwama, M.; Tokura, Y. *Phys. Rev. B* **2003**, *68*, 100406.
(6) Yan, J.-Q.; Zhou, J.-S.; Goodenough, J. B. *Phys. Rev. B* **2005**, *72*, 094412.
(7) Goodenough, J. B. *Nature* **2000**, *404*, 821.
(8) (a) Ye, J.; Zou, Z.; Arakawa, H.; Oshikiri, M.; Shimoda, M.; Matsushita, A.; Shishido, T. *J. Photochem. Photobiol., A* **2002**, *148*, 79. (b) Zhang, L.; Fu, H.; Zhang, C.; Zhu, Y. *J. Solid State Chem.* **2006**, *179*, 804. (c) Mahapatra, S.; Madras, G.; Row, T. N. G. *Ind. Eng. Chem. Res.* **2007**, *46*, 1013.
(9) Reid, A. F.; Sienko, M. J. *Inorg. Chem.* **1967**, *6*, 521.
(10) Alonso, J. A.; Casais, M. T.; Martinez-Lope, M. J. *Dalton Trans.* **2004**, *9*, 1294.
(11) Lundgren, R. J.; Cranswick, L. M. D.; Bieringer, M. *J. Solid State Chem.* **2006**, *179*, 3599.
(12) (a) Bleaney, B.; Pfeffer, J. Z.; Wells, M. R. *J. Phys.: Condens. Matter* **1997**, *9*, 7469. (b) Bowden, G. J. *Aust. J. Phys.* **1998**, *51*, 201. (c) Wang, N.; Zhang, Q.; Chen, W. *Cryst. Res. Technol.* **2007**, *42*, 138.
(13) (a) Rambabu, U.; Amalnerkar, D. P.; Kale, B. B.; Buddhudu, S. *Mater. Res. Bull.* **2000**, *35*, 929. (b) Buissette, V.; Huignard, A.; Gacoin, T.; Boilot, J.-P.; Aschehoug, P.; Viana, B. *Surf. Sci.* **2003**, *532*, 444. (c) Yan, B.; Su, X.-Q. *Opt. Mater.* **2007**, *29*, 547.

Published on Web 10/21/2009

distances with decreasing A^{3+} cation size has been reported for the zircon phases.[14] At pressures of a few kilobars and temperatures less than 600 °C the zircon type vanadates transform to the denser scheelite structures, making them suitable candidates for the investigation of polymorphism among ABO_4-type compounds.[14] Previous investigations of AVO_3 bixbyite oxidations reported the occurrence of $AVO_{3.5+y}$ ($0.00 \leq y \leq 0.22$) intermediate phases during topotactic reactions.[10,15] In contrast, the corresponding perovskites undergo oxidation to the zircon type products with no observable intermediate phases.[15] Intrigued by the presence of the oxidation intermediate $ScVO_{3.5+y}$ during $ScVO_3$ oxidation we decided to investigate this process further using in situ diffraction and thermal analytical methods. In situ techniques are particularly suitable for the detailed understanding of solid state reaction pathways. Frequently ex situ investigations cannot provide equivalent information and are prone to missing significant intermediates. Using in situ methods we can prove the occurrence of intermediates which are subsequently prepared as bulk samples after optimization of the preparative methods. Only very few defect zircon structures such as $RE_{0.9}CrO_{3.85}$ (RE = Gd, Yb, Y)[16] have been reported and those are limited to simultaneous A-cation and anion deficiencies; that is, the B-cation oxidation state is unaltered. Anion deficient structures contain only partially occupied energetically equivalent oxide-ion lattice sites, which are required for good oxide-ion conductivity. These materials find practical applications as solid state ion conductors in solid oxide fuel cells (SOFC) and solid oxide electrolyser cells (SOEC).

There are only four distinct compounds, namely, Sc_2VO_5, $ScVO_4$, $ScVO_3$, and $ScVO_{3.5+y}$ ($0.00 \leq y \leq 0.22$), reported so far in the scandium vanadium oxygen phase diagram. We are reporting for the first time the existence of the metastable oxidation intermediate $ScVO_{4-x}$ which was revealed by in situ powder X-ray diffraction and simultaneous TGA/DTA experiments. It is important to note that the oxidation from $AVO_{3.5+y}$ ($0.00 \leq y \leq 0.22$) to AVO_4 is not topotactic or starting material dependent and involves complete reconstruction of the crystal lattice. The cation disordered bixbyite structures are built from oxygen bridged cation−oxygen octahedra, whereas the zircon structure consists of isolated vanadium−oxygen tetrahedra. The oxygen deficient $ScVO_{4-x}$ zircon structure has been synthesized via low temperature oxidation of $ScVO_{3.5+y}$ ($0.00 \leq y \leq 0.22$). $ScVO_{4-x}$ crystallizes in space group $I4_1/amd$ (141) and maintains the tetragonal zircon structure with disordered oxide defects.

2. Experimental Section

Bulk samples were prepared via a four-step solid state reaction synthesis. All materials were ground in acetone using an agate mortar and pestle. Polycrystalline $ScVO_4$ was synthesized from stoichiometric amounts of Sc_2O_3 (Alfa Aesar: 99.99%) and NH_4VO_3 (Cerac: 99.9%) in air at 1000 °C for 12 h with one intermediate grinding, eq 1

$$Sc_2O_3 + 2NH_4VO_3 \rightarrow 2ScVO_4 + 2NH_3 + H_2O \quad (1)$$

No impurities or traces of starting materials were observed by powder X-ray diffraction. The polycrystalline $ScVO_4$ was then reduced in a CO/Ar (1:3 volume ratio) flow at 600 °C for 12 h, eq 2

$$ScVO_4 + CO \rightarrow ScVO_3 + CO_2 \quad (2)$$

The phase pure $ScVO_3$ was then oxidized topotactically in air at 300 °C for 4 h according to eq 3

$$4ScVO_3 + (1 + 2y)O_2 \rightarrow 4ScVO_{3.5+y} \quad (3)$$

$ScVO_{3.5+y}$ was partially oxidized to $ScVO_{4-x}$ at 500 °C for 12 h in flowing O_2, eq 4

$$4ScVO_{3.5+y} + (1 - 2y - 2x)O_2 \rightarrow 4ScVO_{4-x} \quad (4)$$

Fully oxidized $ScVO_4$ powder was prepared directly from $ScVO_3$ in oxygen flow at 1100 °C, eq 5.

$$2ScVO_3 + O_2 \rightarrow 2ScVO_4 \quad (5)$$

All polycrystalline products were identified with a Bragg-Brentano powder X-ray diffractometer (PANalytical X'Pert Pro, diffractometer radius = 240 mm) using Cu $K\alpha_{1,2}$ radiation (λ = 1.54098 Å, 1.544426 Å) equipped with a diffracted beam Ni-filter and an X'Celerator detector. Room temperature data sets were collected in the 2θ range 10° to 90° in 0.0083° steps using a zero background quartz sample holder. All diffractograms were analyzed by the Rietveld method using GSAS.[19]

In situ powder X-ray diffraction experiments were carried out on the same diffractometer using an Anton Paar HTK2000 high temperature attachment equipped with a platinum strip heater. The 20 min diffractograms were recorded for the angular range 2θ = 8° to 79° using 0.0167° steps. Samples were mounted as thin layers from acetone slurries and heated in oxygen flow from 30 °C to 1000 °C at 10 °C increments. The in situ reduction of $ScVO_4$ in CO/He (1:2 volume ratio) flow was carried out in 20 °C increments from 20 °C to 900 °C. The temperature of the furnace is accurate within at least 5°C between room temperature and 1200 °C.

Powder neutron diffraction data were collected on the medium resolution 800 wire diffractometer C2 operated by the National Research Council Canada at Chalk River at room temperature.[17,18] Diffractograms were measured using a cylindrical vanadium sample container and neutron wavelengths λ = 2.37043(5) Å (5° ≤ 2θ ≤ 85°) and λ = 1.33003(2) Å (35° ≤ 2θ ≤ 115°) at 0.05° increments. Rietveld refinements against powder X-ray and two powder neutron data sets were performed with GSAS.[19] The two neutron wavelengths were refined during the three histogram refinements.

Simultaneous thermogravimetric analysis (TGA) and differential thermal analysis (DTA) experiments were conducted with a Linseis L81 thermobalance. Polycrystalline samples were either fully oxidized in O_2 or fully reduced in CO/Ar with a linear heating rate of 25 °C/min from 25 °C to 1200 °C. All experiments were corrected for buoyancy and were conducted in alumina crucibles with Al_2O_3 powder (similar mass as the sample) as the reference. All products were identified by powder X-ray diffraction.

(14) Chakoumakos, B. C.; Abraham, M. M.; Boatner, L. A. *J. Solid State Chem.* **1994**, *109*, 197.
(15) Shafi, S. P.; Lundgren, R. J.; Cranswick, L. M. D.; Bieringer, M. *J. Solid State Chem.* **2007**, *180*, 3333.
(16) Akoi, Y.; Konno, H. *J. Mater. Chem.* **2001**, *11*, 1458.
(17) Cranswick, L. M. D.; Donaberger, R. L. *J. Appl. Crystallogr.* **2008**, *41*, 1038.
(18) Cranswick, L. M. D.; Donaberger, R.; Swainson, I. P.; Tun, Z. *J. Appl. Crystallogr.* **2008**, *41*, 373.
(19) Larson, A. C.; von Dreele, R. B. *General Structure Analysis System*; Los Alamos National Laboratory Report LAUR 86-748 (2004); Los Alamos National Laboratory: Los Alamos, NM, 2004.

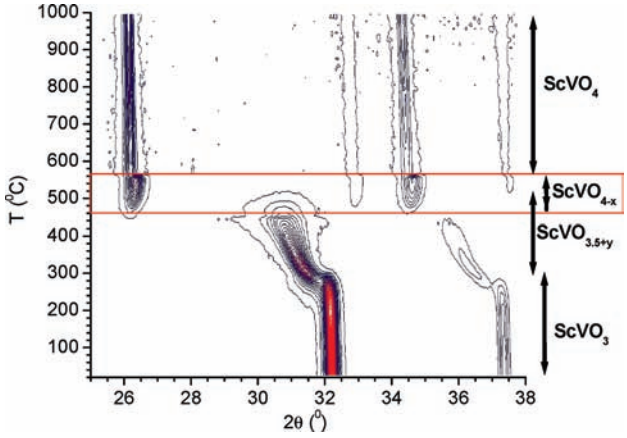

Figure 1. In situ powder X-ray diffraction contour plot of $ScVO_3$ oxidation in oxygen flow from 30 °C to 1000 °C at 10 °C increments. Note the occurence of three transitions. The intensities of the contour lines are shown as constant increments from blue (lowest intensity) to red (highest intensity).

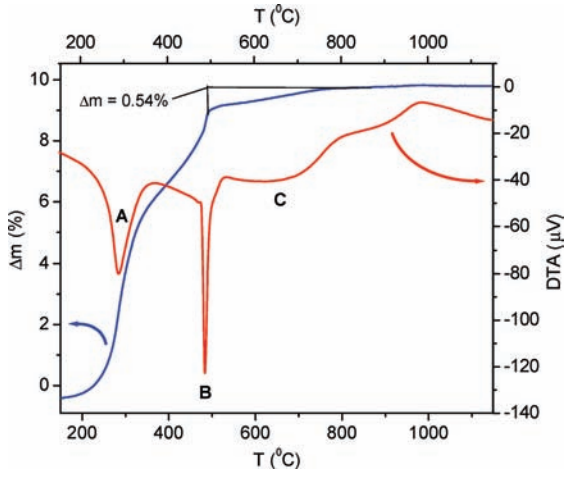

Figure 2. TGA/DTA data showing the oxidation of $ScVO_3$ in oxygen using a heating rate of 25 °C/min. Three exotherms, which are correlated with mass gains, are clearly visible and can be assigned to the oxidation sequence $ScVO_3 \rightarrow ScVO_{3.5+y} \rightarrow ScVO_{4-x} \rightarrow ScVO_4$. The individual features are discussed in the text.

Bulk d.c. magnetic susceptibility measurements were carried out with a Quantum Design MPMS SQUID magnetometer in the temperature range from 2 K to 325 K and using a magnetic field of 0.1 T. The samples were contained in gelatin capsules held in plastic straws. All data were corrected for core diamagnetism and diamagnetic contribution of the gelatin capsules.

Vanadium-51 (157.8 MHz) and scandium-45 (145.7 MHz) NMR were acquired on a Varian Inova 600 (14.1 T) spectrometer using a Varian-Chemagnetics MAS 3.2 mm double-resonance X-H(F) probe. Samples (37 to 41 mg) were ground to a fine powder using an agate mortar and pestle and placed into a 3.2 mm (outer diameter) zirconia rotor (22 μL volume). Ambient temperature (25 °C) ^{51}V MAS spectra were acquired using a single-pulse (Bloch) sequence spinning at 22 000 ± 5 Hz, collecting 256 co-added transients using a 22° tip angle (υ_{rf} = 54 kHz). ^{45}Sc MAS spectra were acquired as described for vanadium using a 14° tip angle (υ_{rf} = 32 kHz). T_1 measurements were performed for ^{51}V using a saturation recovery sequence ($\{90°\}_n - \tau - 90°$) with a saturation comb of n = 24 pulses, spinning at 18 000 ± 3 Hz, using a 1.8 μs 90° pulse. The spectra were referenced to a 0.16 M solution of $NaVO_3$ (−574 ppm with respect to $VOCl_3$) and 0.1 M solution of $ScCl_3$ (0 ppm).[20]

3. Results and Discussion

a. Oxidation Pathway of $ScVO_3$. $ScVO_3$ crystallizes in the cubic bixbyite structure, space group $Ia\bar{3}$ (206) with scandium/vanadium disorder on the 8*b* and 24*d* sites.[9,10] In situ powder X-ray diffraction experiments, Figure 1, and simultaneous thermogravimetric/differential thermal analysis (TGA/DTA) data, Figure 2, of $ScVO_3$ oxidation in oxygen flow indicate that the oxidation to $ScVO_4$ proceeds through at least two intermediate phases. In agreement with earlier reports,[10,15] the cubic bixbyite phase $ScVO_3$ undergoes a topotactic oxidation to the defect fluorite structure $ScVO_{3.5+y}$ ($0.00 \leq y \leq 0.22$), space group $Fm\bar{3}m$ (225). This process is evident from the contour plot of the in situ powder X-ray diffraction experiments at approximately 300 °C, that is, the disappearance of the bixbyite peaks accompanied by the appearance of the defect fluorite peaks. The exothermic peak A and the associated mass gain in the TGA/DTA data in Figure 2 are in agreement with this reaction step. The defect fluorite structure, $ScVO_{3.5+y}$, is made up from $(1-2y)V^{4+}$ and $(2y)V^{5+}$ cations, and all cations, that is, Sc^{3+}, V^{4+}, and V^{5+}, are disordered on the 4*a* site.[10,15] At approximately 450 °C the fluorite structure disappears, and a tetragonal phase consistent with space group $I4_1/amd$ similar to the zircon structure $ScVO_4$ is observed in the in situ X-ray diffraction experiment, Figure 1. The exotherm B and the associated mass gain in this temperature range in Figure 2 agree with this oxidation step. The apparent sudden shift (ΔT = 10 °C, Δt = 20 min) of the tetragonal peaks towards lower diffraction angles with no evidence of a space group change at 570 °C indicates unit cell expansion. In fact, the peaks show significant sharpening while shifting toward lower diffraction angles. We propose that the intermediate observed between 450 °C and 570 °C is an oxygen defect zircon structure which undergoes full oxidation to $ScVO_4$ at 570 °C in oxygen. A mass gain of 0.54% (TGA) and a broad exothermic peak C (DTA) between 500 °C and 750 °C in Figure 2 support this additional oxygen uptake during the final reaction step. Note that this transition occurs over a broad temperature range during fast heating in the TGA/DTA experiment while a narrow temperature range is observed for slow heating during the in situ powder X-ray diffraction studies. Notably the diffraction peaks of the defect fluorite and the defect zircon structures are significantly broader than those for the bixbyite starting material and the final zircon structure. This peak broadening is associated with the presence of defects and the resulting limited crystallinity of these polycrystalline phases. In summary the thermogravimetric/differential thermal analysis (TGA/DTA) data and in situ powder X-ray diffraction data suggest that oxidation of $ScVO_3$ follows the sequence $ScVO_3 \rightarrow ScVO_{3.5+y}$ ($0 \leq y \leq 0.22$) $\rightarrow$ $ScVO_{4-x}$ ($x \leq 0.10$) $\rightarrow$ $ScVO_4$. The total mass gain during oxidation indicates that the starting material was $ScVO_{3.07(2)}$ and the third oxidation step with 0.54 % mass gain suggests that the oxygen stoichiometry of the intermediate zircon defect structure is $ScVO_{3.91(2)}$.

(20) Mason, J. *Multinuclear NMR*; Plenum Press: New York, 1987.

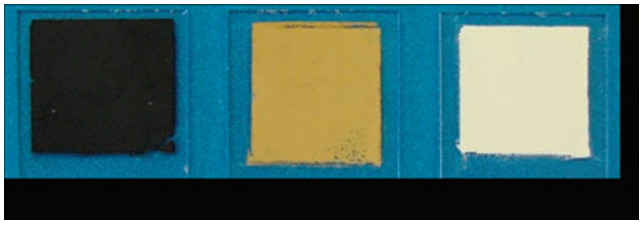

Figure 3. Comparison of black $ScVO_{3.70}$, beige $ScVO_{3.94}$, and white $ScVO_{4.00}$ sample colors.

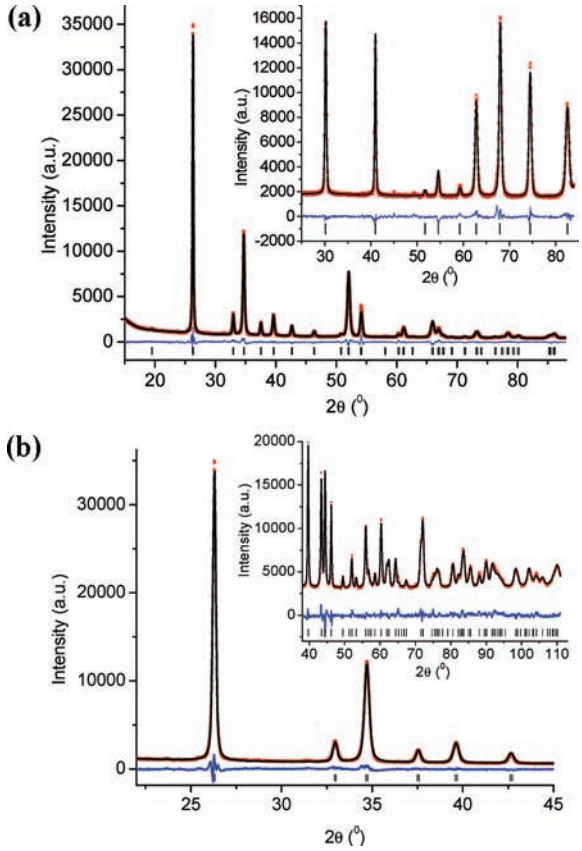

Figure 4. Rietveld plots of $ScVO_{3.94}$ room temperature refinement. (a) Powder X-ray diffraction data with Cu $K\alpha_{1,2}$ radiation and powder neutron diffractogram (inset) with λ = 2.37126(5) Å. Red crosses = experimental data, black line = best fit, blue line = difference, black tick marks = Bragg positions. (b) Low angle range of powder X-ray diffraction data with Cu $K\alpha_{1,2}$ radiation and short wavelength powder neutron diffractogram (inset) with λ = 1.32967(2) Å. Red crosses = experimental data, black line = best fit, blue line = difference, black tick marks = Bragg positions.

b. $ScVO_{4-x}$ Bulk Sample. Phase pure bulk samples of $ScVO_{4-x}$ were obtained from single phase $ScVO_{3.5+y}$ starting materials. It is noteworthy that samples prepared directly from $ScVO_3$ resulted in impure products containing $ScVO_{3.5+y}$. $ScVO_{3.5+y}$ is a black powder, $ScVO_{4-x}$ is yellowish-brown, and $ScVO_4$ is cream colored: the contrasting sample colors are shown in Figure 3. The oxygen stoichiometry of the oxygen defect bulk sample was confirmed to be $ScVO_{3.94(2)}$ using TGA under oxidizing ($ScVO_{4-x} + (x/2)O_2 \rightarrow ScVO_4$) and reducing ($ScVO_{4-x} + (1-x)CO \rightarrow ScVO_3 + (1-x)CO_2$) conditions and was compared with fully oxidized $ScVO_4$ with no oxygen uptake during oxidation and an oxygen stoichiometry of $ScVO_{3.99(1)}$ as determined during reduction.

Table 1. Structural Parameters, Bond Angles, and Average Bond Distances for $ScVO_{4-x}$ Zircon Defect Phase (space group: $I4_1/amd$) As Obtained from Rietveld Refinements against Two Neutron and One X-ray Diffraction Pattern Measured at Room Temperature[a]

T (K)		296 K
unit cell	a (Å)	6.77761 (5)
	c (Å)	6.14045 (8)
	V (Å^3)	282.067(5)
Sc (4a)	$U_i/U_e \times 100$	1.35
	occ.	1.000
V (4b)	$U_i/U_e \times 100$	2.85
	Occ.	1.01(3)
O1 (16h)	x/a	0
	y/b	0.4425 (1)
	z/c	0.1971 (1)
	$U_i/U_e \times 100$	1.33
O−V−O (deg)		114.34(3)
		100.12(5)
d(V−O) (Å)		4 × 1.7014(7)
O−Sc−O (deg)		
d(Sc−O) (Å)		4 × 2.1308(7)
		4 × 2.3694 (7)
composition (TGA)		$ScVO_{3.94(2)}$
no. of parameters		11
R_p: XRD		4.19
NPD λ = 2.37126(5) Å		3.16
NPD λ = 1.32967(2) Å		3.19
powder totals		3.70
R_{wp}: XRD		5.56
NPD λ = 2.37126(5) Å		4.40
NPD λ = 1.32967(2) Å		4.17
powder totals		4.96
$R(F^2)$: XRD		12.20
NPD λ = 2.37043(5) Å		3.56
NPD λ = 1.33003(2)Å		11.88
χ^2: powder totals		4.031

[a] Sc^{3+} is located on site 4a (0, 3/4, 1/8) and V^{5+} on 4b (0, 1/4, 3/8).

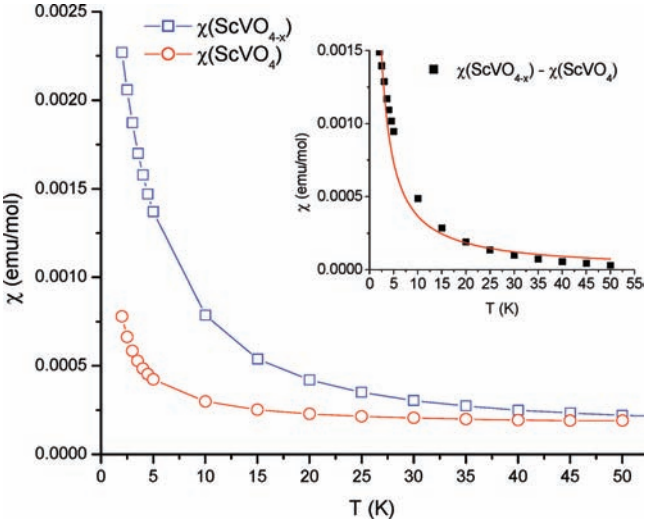

Figure 5. Bulk d.c. magnetic susceptibility data of $ScVO_4$ and $ScVO_{4-x}$ measured in a magnetic field of H = 0.1 T, corrected for core diamagnetism. The inset shows the temperature dependent d.c. magnetic susceptibility of $ScVO_{4-x}$ after subtraction of the $ScVO_4$ susceptibility; the solid line is the Curie fit.

The combined Rietveld refinement against one powder X-ray and two powder neutron diffractograms revealed that $ScVO_{4-x}$ can be described as a zircon structure. Unfortunately, the diffraction data sets did not permit quantification of the minute oxygen defect concentrations. Nevertheless, the average crystallographic structure has been unambiguously identified as a zircon

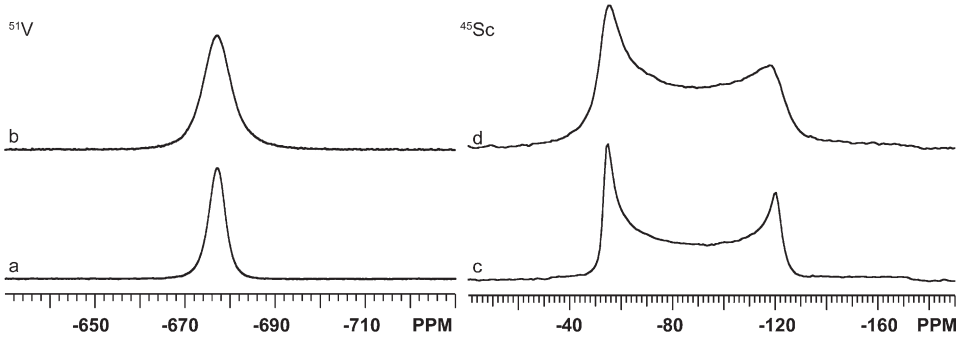

Figure 6. ^{51}V and ^{45}Sc MAS NMR central transition peaks for $ScVO_4$ (a, c) and $ScVO_{4-x}$ (b, d).

structure with very reasonable bond lengths and structural parameters during the multi-histogram refinements against powder X-ray and neutron diffraction data: the Rietveld plots are shown in Figure 4. The backgrounds were fitted with a cubic spline between background points during an early stage of the refinement but were held fixed during the final refinement cycles. The tetragonal unit cell constants, all zero points and peak shape parameters for the pseudo-Voigt functions, were refined together with the atomic coordinates of oxygen and all aniosotropic temperature factors. The structural details are provided in Table 1. In contrast to the earlier reported defect fluorite structures, $ScVO_{3.5+y}$ ($0 \leq y \leq 0.22$),[15] the powder neutron diffraction data of $ScVO_{4-x}$ did not reveal any evidence of oxygen defect clustering.

Temperature dependent d.c. magnetic susceptibilities of the fully oxidized $ScVO_4$ sample were subtracted from magnetic susceptibilities of the $ScVO_{4-x}$ defect zircon structure. The resulting difference revealed a small paramagnetic signal consistent with small amounts of V^{4+} in the otherwise diamagnetic compound. Note that $ScVO_4$ and $ScVO_{4-x}$ both showed the typical paramagnetic temperature dependence due to miniscule amounts of paramagnetic impurities in the starting materials; subtracting the fully oxidized sample data from the defect structure data eliminates the magnetic signal from the starting material impurities, and thus the remaining signal represents V^{4+} paramagnetism in the defect structure, Figure 5. The deviations from the Curie fit shown in the inset of Figure 5 are most likely caused by small differences of the sample holders used for the two experiments. The d.c. magnetic susceptibility is consistent with a minimum of 3% of V^{4+} in the sample.

Magic angle spinning solid state NMR spectroscopy revealed significantly broader ^{51}V peaks for V^{5+}-O_4 tetrahedral environments in the oxide defect structure $ScVO_{4-x}$ (1110 Hz), Figure 6b, than for the fully oxidized $ScVO_4$ sample (655 Hz), Figure 6a. This broadening could be due to increased disorder in the structure or to the presence of paramagnetic centers. However, the ^{51}V spin−lattice relaxation times (T_1) decreased dramatically from 25(1) s to 1.0(1) s for the defect structure, betraying the influence of paramagnetic cations. Furthermore, the absolute (mass-normalized) integrated ^{51}V signal intensity decreased by approximately 7% from $ScVO_4$ to $ScVO_{4-x}$, supporting the reduction of V^{5+} to paramagnetic V^{4+} in the defect sample to form $ScVO_{3.94}$. The ^{45}Sc solid state NMR spectrum for $ScVO_4$, Figure 6c, agrees with the data published by Kim et al.[21] of 8-fold coordinated scandium in $ScVO_4$ ($\delta_{iso} = -33(1)$ ppm, $C_Q = 21.6(1)$ MHz, $\eta \leq 0.05$). In $ScVO_{4-x}$, the ^{45}Sc peak broadens by approximately 9 ppm (1300 Hz) due to the proximity of paramagnetic V^{4+}, Figure 6d, and a corresponding reduction in relaxation times is observed.

To evaluate the reversibility of the reduction−oxidation cycle between $ScVO_4$ and $ScVO_3$ the in situ powder X-ray diffraction reduction of $ScVO_4$ in flowing CO/He was followed. During this reduction no evidence of the formation of any intermediates was observed. The reaction occurs in a single step between 650 °C and 750 °C as seen in the in situ X-ray diffraction data, Figure 7. Figure 8 shows the TGA/DTA traces during the reduction of $ScVO_4$ to $ScVO_3$ in CO/Ar with a single broad exotherm and a single step mass loss. This oxidative versus reductive hysteresis demonstrates that the $ScVO_{3.5+y}$ and $ScVO_{4-x}$ phases are only formed from appropriate starting materials, that is, during gentle oxidation, but that they cannot be accessed directly via reduction of $ScVO_4$ using conventional methods. This serves as evidence of a strong structure−reactivity relation in the zircon−bixbyite system. In addition to the in situ diffraction experiments $ScVO_3$ oxidation reactions were carried out at 500 °C in air and pure oxygen flow for 24 and 36 h and resulted in the partially oxidized yellowish-brown $ScVO_{4-x}$ defect phase. Reduction of $ScVO_4$ in carbon monoxide at 500 °C for 24 h resulted in the formation of fully reduced black $ScVO_3$.

The three steps of the oxidative pathway from $ScVO_3$ to $ScVO_4$ can be rationalized in terms of structural similarities during the topotactic processes as well as major lattice reconstructions for the non-topotactic steps due to poorly matching ionic radii. $ScVO_3$ undergoes oxidation by means of topotactic oxygen uptake at low temperatures. The bixbyite structure is formally a largely oxygen deficient fluorite structure with 25% of ordered oxide defects. $ScVO_{3.5+x}$ with $0 \leq x \leq 0.22$ is an oxygen defect fluorite structure that can accommodate disordered oxide defects with concentrations ranging from 12.5% ($ScVO_{3.5}$) to 7% ($ScVO_{3.72}$). The large concentration of the small V^{5+} cation (44%) for $ScVO_{3.72}$ destabilizes the defect fluorite structure and results in the formation of an oxygen deficient zircon structure $ScVO_{4-x}$. The reconstructive oxidative transition involves major cation reorganization. The final oxidative step follows a topotactic route such that the disordered oxide defect positions will be filled with oxide anions resulting in stoichiometric $ScVO_4$. Figure 9a shows the cation positions in bixbyite

(21) Kim, N.; Hsieh, C.-H.; Stebbins, J. F. *Chem. Mater.* **2002**, *18*, 3855.

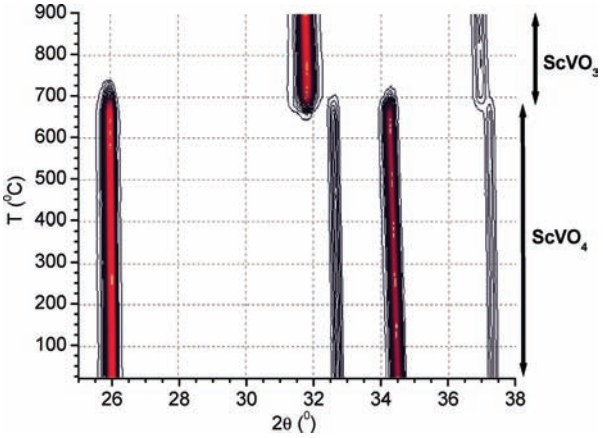

Figure 7. In situ powder X-ray diffraction contour plot of $ScVO_4$ reduction in CO/Ar flow from 20 °C to 900 °C at 20 °C increments. The reduction proceeds in a single step from $ScVO_4$ to $ScVO_3$. Diffraction peak intensities are shown as constant increment contours from blue (lowest intensity) to red (highest intensity).

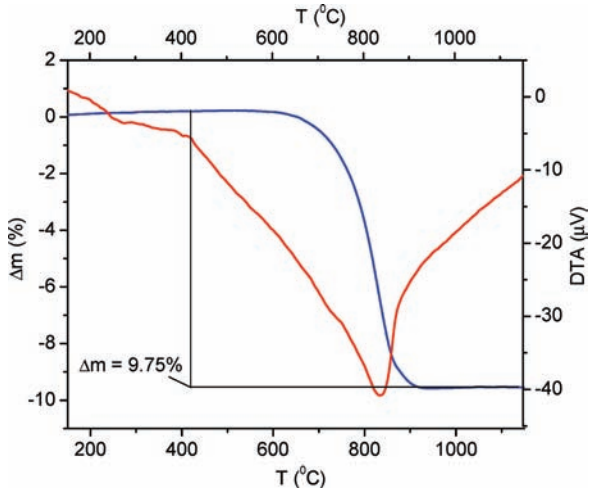

Figure 8. TGA/DTA reduction of $ScVO_4$ in CO/Ar flow using a heating rate of 25 °C/min. Only one broad exotherm and mass loss due to the single step reduction of $ScVO_4$ to $ScVO_3$ is observed; the mass loss corresponds to $ScVO_{3.02}$ formation.

(red spheres) and fluorite (green spheres); the coordinates have been adjusted to provide a common origin for both structures. It is evident from Figure 9a that there are only subtle changes in the cation positions during the transition from the bixbyite to the fluorite structure, thus emphasizing the topotactic nature of the reaction step. This topotactic oxidation of $ScVO_3$ to $ScVO_{3.5+y}$ has been reported in the past.[10,15] In contrast the oxidation from the defect fluorite ($ScVO_{3.5+y}$) to the defect zircon structure ($ScVO_{4-x}$) requires a major lattice reconstruction. Figure 9b illustrates the relationship of the cation lattices between the fluorite and the zircon structure as observed during oxidation. The disordered Sc^{3+} and V^{3+} cations (green spheres) in the fluorite type structure separate into two distinct cation lattices and form two interpenetrating distorted diamond sublattices in the zircon structure (Sc^{3+} = blue, V^{3+} = yellow). Here we also report the oxide deficient zircon type $ScVO_{4-x}$ structure and its oxidative formation for the first time. We propose that during oxidation the defect fluorite structure collapses and that the oxide defect zircon structure is

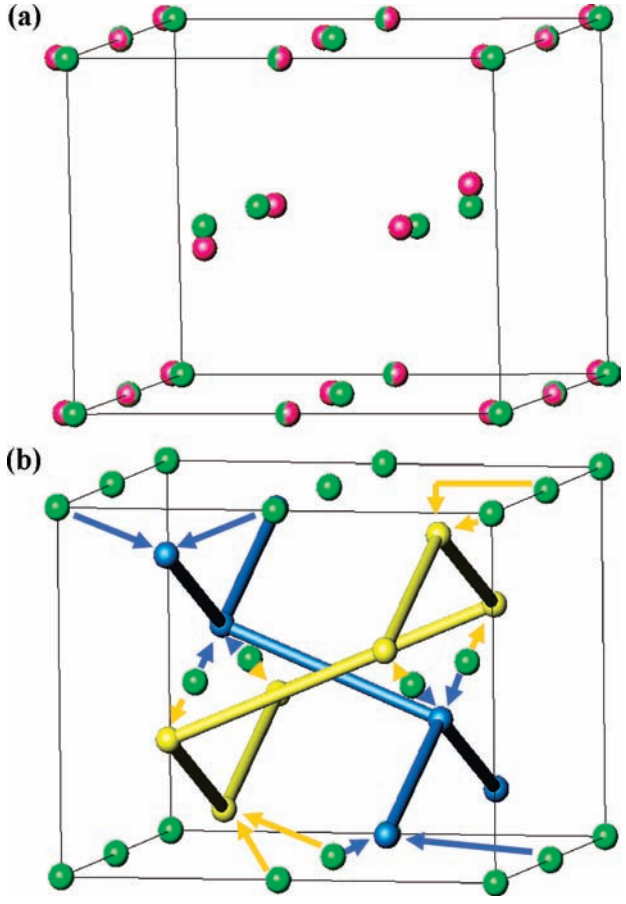

Figure 9. (a) Schematic illustration of cation movement during the transition from bixbyite to fluorite structure. Green = disordered cations in fluorite structure; red = disordered cations in bixbyite structure. All oxide positions have been omitted for the sake of clarity. (b) Schematic illustration of reconstruction of the cation network during the structural transition from fluorite to zircon. Green = disordered cations in fluorite structure; blue, yellow = ordered cation network in the zircon structure. All oxide positions have been omitted for the sake of clarity.

initially assembled with sufficient oxide and V^{5+} concentrations to build a sustainable oxide network. During the final oxidation step the oxide vacancies in $ScVO_{4-x}$ are filled topotactically, resulting in stoichiometric $ScVO_4$. This mechanism appears to be driven by the V^{5+} cation size. Pentavalent vanadium is too small to be accommodated in the fluorite structure. Notably the final oxygen uptake is a distinct step from the initial zircon network formation. This contrasts with a formation mechanism involving oxygen inhomogeneities through phase fraction changes of $ScVO_{3.5}$ and $ScVO_4$.

4. Conclusion

We have reported the synthesis, structure description, and thermal stability of the novel defect zircon phase $ScVO_{4-x}$. The oxidation of $ScVO_3$ proceeds through the topotactic formation of $ScVO_{3.5+y}$ ($0.00 \leq y \leq 0.22$) defect fluorite, followed by the occurrence of the novel $ScVO_{4-x}$ ($x \leq 0.1$) defect zircon phase, and completes with the topotactic oxidation to the $ScVO_4$ zircon phase. The structure−reactivity relationship is evident from the contrasting single step reduction of $ScVO_4$ to $ScVO_3$ with no observable intermediates. Consequently, following an appropriate route permits the formation of novel phases with variable oxidation states;

this is a significant step forward for solid state synthetic methods. The phase transition from the defect fluorite to the defect zircon structure is not driven by oxygen affinity but by the decreasing average B-cation size during oxidation. In situ methods have been crucial for the discovery of these reaction pathways and will likely provide important insights into solid state reactivity in the future.

Acknowledgment. We are grateful to NSERC of Canada for operating and infrastructure support (M.B., S.K.) and a graduate scholarship (V.K.M.). The Canada Foundation for Innovation is acknowledged for providing the NMR and XRD facilities. We thank Craig Bridges (McMaster University) for assistance with the magnetic measurements.